Powder Technology 443 (2024) 119873

Contents lists available at ScienceDirect

Powder Technology

journal homepage: www.journals.elsevier.com/powder-technology

Discrete element modelling of the elastic-plastic and viscoelastic properties of a lithium-ion battery electrode layer

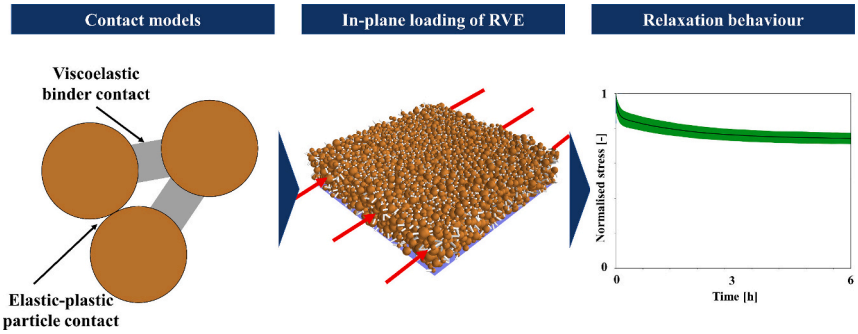
Axel Lundkvist [a], Per-Lennart Larsson [a], Anand H.S. Iyer [a,b], Erik Olsson [c,*]

[a] Department of Engineering Mechanics, Division of Material and Structural Mechanics, KTH Royal Institute of Technology, Teknikringen 8, 100 44 Stockholm, Sweden
[b] Testing Department, Jotun Performance Coatings, Jotun A/S, Sandefjord, Norway
[c] Department of Engineering Sciences and Mathematics, Division of Solid Mechanics, Luleå University of Technology, Luleå, Sweden

HIGHLIGHTS

- DEM model capturing Li-battery electrode's mechanical properties is implemented.
- An active particle contact model based on contact mechanics is used.
- Relaxation simulations are performed utilizing a viscoelastic binder contact model.

GRAPHICAL ABSTRACT



ARTICLE INFO

Keywords:
Lithium-ion batteries
Discrete element method
Simulations
Mechanical characterisation
Contact mechanics
Viscoelasticity
Relaxation

ABSTRACT

Mechanical degradation mechanisms are one of the leading causes of charge capacity loss in lithium-ion batteries. This study further develops a discrete element method (DEM) simulation framework, which investigates how the local contact behaviour affect the global mechanical properties of the active layer. The local microstructure consists of active particles held together by a binder domain, making up a granular medium. This study investigates the impact of the layer's global properties from the type of particle contact model. Experiments were also performed to measure size distribution and the material properties of the active material. The time dependency of the active layer, stemming from the viscoelastic binder domain, was studied in relaxation simulations, which were based on experimental measurements.

1. Introduction

The transition from fossil fuels to green and sustainable energy systems is a crucial step in the mission to mitigate climate change. Lithium-ion batteries (LIB) play a significant role in the green energy storage systems of the future, and extensive research and development have been made in the field over the last decades [1]. Historically, the main research focus has been on the development of the battery chemistry. However, the performance of LIBs is also affected by their mechanical properties, and therefore, the mechanical properties of LIBs is an

* Corresponding author.
E-mail address: erik.1.olsson@ltu.se (E. Olsson).

https://doi.org/10.1016/j.powtec.2024.119873
Received 18 January 2024; Received in revised form 7 May 2024; Accepted 15 May 2024
Available online 18 May 2024
0032-5910/© 2024 The Authors. Published by Elsevier B.V. This is an open access article under the CC BY license (http://creativecommons.org/licenses/by/4.0/).

important topic of interest [2]. LIBs consist of a stack of thin positive and negative electrode layers, which are prevented from short-circuiting by a porous separator. A liquid electrolyte connects the two electrodes and enables the electrochemical reaction, where lithium ions are transported between the two electrodes. The electrode layers are comprised of electrochemical active particles, which are held together by a conductive carbon binder domain (CBD) and connected to the external circuit by a thin metal current collector. The negative electrode generally uses graphite as its active material (AM), while several metal oxides, e.g. lithium nickel manganese cobalt oxide (NMC), can be used in the positive electrode. The CBD is comprised of polyvinylidene fluoride (PVDF) mixed with conductive carbon black (CB). During the charging/discharging process, lithium ions intercalate/deintercalate in and out of the AM in the positive and negative electrodes.

Some of the current challenges in developing LIBs include increasing the charge capacity and charging rates while reducing the charge capacity degradation over cycling. Charge capacity loss is a complex phenomenon where several electrochemical and mechanical phenomena interact. One process driving the charge capacity degradation is active particle cracking in the positive electrode due to the lithium-ion intercalation/deintercalation process during discharging/charging. The intercalation of lithium ions causes the active particles to swell, and deintercalation returns them to their original size. Over several charge and discharge cycles, this repeated swelling causes cracking of the active particles. The repeated swelling also affects the electrode layer with damage in the CBD, causing delamination of the electrode layer from the current collector and island formation within the electrode layer [3,4].

Numerical modelling tools are essential for investigating the LIB's mechanical properties and degradation mechanisms. They can extend the results from experimental observations while also providing information on the mechanical properties that cannot be obtained through experiments. For simulations on the electrode layer scale, the discrete element method (DEM) has proven to be applicable as the active particles and CBD build up a granular microstructure. In the literature, the primary focus has been on the calendering process during manufacturing [5–14], but other properties and processes have also been investigated. The lesser-covered topics comprise the active layer drying process, AM particle flow for solvent-free electrode production, electrical and ionic conductivity, and heat transfer in the active layer [15–20]. Schreiner et al. [5–7] developed a DEM framework for modelling the calendering process of LIB cathodes to determine optimal calendering parameters, particularly the electrodes' final porosities dependence on the roll gap width. Sangrós Giménez et al. [8,15–17] study several aspects of LIB active layers using DEM. Initially, a methodology was developed for reproducing the granular microstructure and properties such as porosity, particle size distribution, and layer thickness were validated against experimental results [15]. The calendering process was also investigated, focusing on the layers' final porosity and thickness, the elastic spring-back of the layer height and the contact area between the active particles and the current collector [8]. The impact of the calendering process was also linked to the electrochemical properties of the electrode layer, mainly the ionic and electrical conductivity. Following the calendering, the impact of electrochemical cycling on the mechanical properties of the layers was investigated. This was done by coupling the active particle size and material properties to their state of charge and tracking the number of contacts per active particle and the mechanical stress in the layer during charge cycling [16]. Lippke et al. [9] investigated the heat flux in the cathode layer during calendering and, in particular, the effect of preheating the layer before calendering to improve the microstructure of the layer after calendering. Zhang et al. [13,14] also applied DEM to study the impact of electrode composition and calendering parameters on the microstructure, mechanical, electronic and heat transfer properties of the electrode layer. Despite this extensive modelling of the positive electrode layer, there is still a missing understanding of its mechanical behaviour, such as its time-dependent mechanical properties, which have not, to the author's knowledge, been explored in the literature.

Accurate model inputs, such as material properties, are vital for modelling the electrode layer. Several experimental methods have been applied to characterise the positive electrode on different length scales. For characterising the AM particles' material properties, nanoindentation and flat punch indentation have been used extensively to determine the NMC materials' modulus, hardness, and fracture strength [2]. For the CBD, which builds up a more complex structure within the electrode layer, several experimental setups have been used to characterise both the CBD and its components separately. The time-dependent deformation behaviour of PVDF, in the form of thin films, has been investigated by Santimetaneedol et al. [21] and Ono [22] via creep, relaxation, and load-unload tests.

The CBD has been tested for how its mechanical properties are affected by its drying process, its composition of polymer binder, CB and crosslinking agents, and from being soaked in electrolytes. The testing is often performed on pure CBD [21,23–26]. The CBD has also been tested in already manufactured electrodes. Iyer et al. [27] applied micromechanical testing to determine the modulus and yield strength of the CBD in an uncycled dry cathode layer. The CBD was assessed using nanoindentation, micropillar compression, and microcantilever bending tests, and the measured properties from the different testing procedures were compared. Vasconcelos et al. [28] measured the CBD mechanical properties in a cathode layer using grid indentation, where both the AM and the CBD were tested in tandem.

The mechanical properties of the complete electrode layer have also been evaluated via various testing methods. Gupta et al. [29] and Üçel al. [30] tested the in-plane unloading properties and relaxations of cathode and anode active layers using a U-shape bending method. Zhang et al. [31] tested the entire cathode, including the current collector, in tensile and compression tests to determine a constitutive model for the active layer. A blunt rod test was also performed on a stack of electrodes, and the test was replicated using finite element analysis. Flat punch indentation of the electrode layer has also been performed as a way of validating simulation models [5,15].

Characterisation of the electrode microstructure is also relevant, as it can explain the mechanical behaviours in the layer, e.g., from the particle contact networks within the layer, and its electrical conductive properties in the form of conductive paths. It also gives vital input to simulations. Ebner et al. [32] used synchrotron radiation X-ray tomographic microscopy to capture the 3D structure of cathode layers with different mass loadings of AM and calendered to different degrees. The size distribution of particles within the layer was captured, as well as damage to the AM in the form of particle cracking. Bond et al. [33,34] studied the structural evolution of and damage in electrodes using computed tomography (CT). By using CT, whole cells could be imaged in situ between charge cycles and the evolution of the electrode structure, such as electrode layer swelling, and damage, such as active particle cracking and electrode layer delamination from the current collector, was captured. Nagda et al. [35] developed a framework for recreating a statistical-equivalent stochastic 3D microstructure for a positive electrode active layer. The framework is based on a machine learning segmentation algorithm trained on tomography data of cathode microstructures published in the literature. This segmentation algorithm provides the input parameters for the 3D microstructure generation model.

In our previous published paper [36], a discrete element method (DEM) simulation framework was developed to investigate the mechanical properties of a positive electrode active layer. The primary outcome of the study was capturing the pressure sensitivity of the layer, where the in-plane unloading stiffness would increase at increased compressive strains and be constant at all strain levels in tension. Building on our previous work, this paper extends the investigation of the mechanical properties of the positive electrode layer through experiments and simulations. The experimental study will comprise the measurement of the particle size distribution (PSD) of the NMC powder

through dynamic image analysis, as well as determining the material properties of the NMC through nanoindentation. Accurate measurements of the NMC material properties will enable theoretically motivated contact models for the particle contact, which have previously been based on compression tests of active particles or calibration of the particle contact model to give correct mechanical properties of the full layer. The contact model used in this study is based on advanced contact mechanics. It provides an accurate contact formulation following the material's mechanical properties, specifically its Young's modulus and yield strength. This also generalises the framework, enabling using different sets of material properties for the active material. Modelling the time-dependent behaviour of the active layer is also a novel part of the work where a viscoelastic contact model for the CBD will be implemented, allowing relaxation simulations to be performed, cohering to the experiments performed by Gupta and Ucel [29,30]. This article initially presents the experimental work, consisting of particle size measurements and the material characterisation of the NMC particles through indentation testing. The experimental section is followed by presenting the active particles' elastic-plastic contact model and the CBD's viscoelastic contact model together with the relevant simulations for each section. The present study aims to establish a solid numerical foundation for analysing the mechanical behaviour at initial packing and calendering and determining the resulting mechanical properties relevant to the positive electrode layer. The numerical foundation is established using the discrete element method and verified from relevant experimental studies. With this framework at hand, features such as particle swelling and cracking, relevant for the analysis of mechanical degradation, can be studied in an accurate manner.

2. Experiments on the active particles

2.1. Particle size measurement

The particle size distribution (PSD) of the NMC powder was determined through dynamic image analysis with results in Fig. 1. The measurement setup consisted of the dynamic image analysis sensor (QICPIC, Sympatec GmbH, Germany), equipped with a dry dispersion system (OASIS/L, Sympatec GmbH, Germany) and a vibratory feeder (VIBRI/L, Sympatec GmbH, Germany). A dispersion pressure of three bar was used during the measurement. The particle diameter, x, was evaluated as the diameter of a circle of equal projection area to the imaged particle (EQPC). The volume-based particle size distribution was determined through the software PAQXOS 5.2.1 (Sympatec GmbH, Germany). The cumulative distribution limits of the measurement of the PSD was $x_{10,3} = 8.29$ µm, $x_{16,3} = 9.10$ µm, $x_{50,3} = 12.63$ µm, $x_{84,3} = 16.82$ µm, $x_{90,3} = 17.73$ µm, and $x_{99,3} = 23.21$ µm for the NMC powder.

2.2. Indentation experiments

The elastic stiffness and hardness of the active material were determined through nanoindentation testing. The sample tested was manufactured from an uncycled positive electrode layer with NMC-622 as active material, PVDF and CB as CBD and an aluminium current collector. CUSTOMCELLS® supplied the sample, and equal samples have previously been used by Gupta et al. [29] and Iyer et al. [27]. The active layer only coated one side of the current collector, and its thickness was 111 µm. The composition of the active layer was 86 wt% active material, 7 wt% PVDF and 7 wt% CB. Two electrode layers were glued together and sandwiched between silicon wafers to get a structurally stable sample. The sample cross-section was prepared with a Leica TIC3X broad ion beam (BIB) polisher in order to obtain a flat indentation surface, and the sample was polished for eight hours at 5.5 kV. The prepared cross-section, with all components highlighted, is shown in Fig. 2.

The nanoindentations were performed using an Alemnis in-situ SEM nanoindenter (Alemnis AG, Switzerland), equipped with a Berkovich diamond tip, and placed in a Zeiss Ultra 55 FEG SEM. The test used a displacement-controlled mode with a maximum indentation depth between 200 and 300 nm. A displacement rate of 20 nm/s was used at loading, and the displacement was held for 10s at the maximum indentation depth to mitigate the influence of material creep. The unload rate was set to 50 nm/s. The modulus and hardness from the indents were determined using the Oliver-Pharr method [37] where the reduced modulus E_r and the unloading stiffness S are related through

$$S = \frac{dP}{dh} = \beta \frac{2}{\sqrt{\pi}} E_r \sqrt{A} \tag{1}$$

where $\frac{dP}{dh}$ is the measured stiffness at unloading from the maximum indentation force P_{max}, β is a dimensionless correction parameter dependent on indentation tip shape, and A is the projected contact area at peak load. The projected area is determined through an indenter type specific shape function

$$A = F(h_c), \tag{2}$$

dependent on the contact depth h_c, which is calibrated on a reference material, in our case a standard fused silica specimen. The reduced modulus and the modulus of the tested material and the indenter ma-

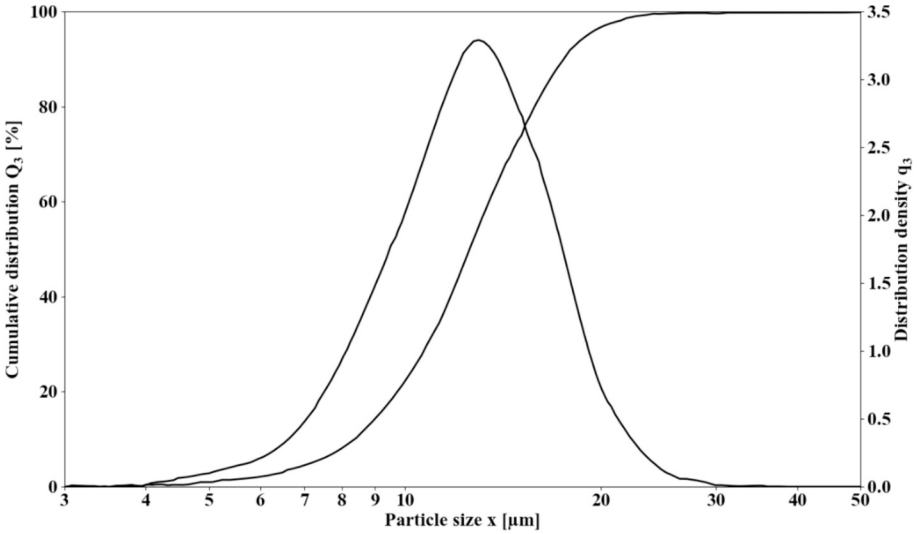


Fig. 1. Cumulative distribution and distribution density of the particle size distribution by volume.

terial are related through

$$\frac{1}{E_r} = \frac{1-\nu^2}{E} + \frac{1-\nu_i^2}{E_i}, \tag{3}$$

where E and ν is the Young's modulus and Poisson's ratio for the specimen material and E_i and ν_i are the elastic constants for the indenter. The diamond Berkovich tip had a modulus $E_i = 1141$ GPa and a Poisson's ratio $\nu_i = 0.07$ and the Poisson's ratio of the tested material was assumed to $\nu = 0.25$. The hardness H of the tested material is estimated through

$$H = \frac{P_{max}}{A}, \tag{4}$$

where A is the projected contact area, presented in Eq. (2). The modulus and hardness for the NMC particles were determined to $E = 47 \pm 3.6$ GPa and $H = 7.2 \pm 0.75$ GPa, respectively. The size of the indents was around 2–3 μm. To avoid influence of the particle-CBD interfaces, only large enough particles (> 10 μm) were selected for indentation. A SEM live image was used to guide the position of the indenter tip towards the centre of the particle. Indents far away from the centre were discarded. The CBD was also investigated through nanoindentation; however this was deemed an inappropriate technique for evaluation of mechanical properties of the CBD [27]. In reference to these results, it should be noted that a more accurate way of determining modulus and hardness would be to evaluate the contact area of the indent through image analysis. However, this was deemed unnecessary for these standard measurements. The hardness is related to the yield strength of the material through

$$H = 3\sigma_Y, \tag{5}$$

as stipulated by Tabor [38]. It should be mentioned that with the material properties presented just above, Eq. (5) will be accurate even though some influence from elastic effects can be expected.

3. Discrete Element Modelling

3.1. NMC particle contact model

In our previous study, the particle contact model was based on experimental studies of the force-overlap relation for the active particles, as given by particle compression experiments [8]. To better understand the contact behaviour and to present a contact model following material properties, elastic-plastic contact theory should be applied. As the active material follows an elastic-plastic behaviour, as shown both in our experiments and the literature, the particle contact model should account for this constitutive behaviour. As stipulated by Johnsson [39], the contact during indentation can be divided into three regions: a fully elastic region, a fully plastic region, and a region where elastic and plastic loading co-occur. To describe the contact during indentation, two dimensionless parameters are used: the normalised hardness $\overline{H}$, defined as

$$\overline{H} = \frac{F}{\pi a^2 \sigma_{rep}}, \tag{6}$$

and the contact area parameter c^2, defined as

$$c^2 = \frac{a^2}{2hR}, \tag{7}$$

where F is the contact force, σ_{rep} is the yield strength at a representative value of the plastic strain, a is the contact radius, R is the radius of the indenter, and h is the indentation depth. In this study the active material is assumed to be perfectly plastic, which entails a constant yield strength. Both parameters can be related to a dimensionless loading parameter Λ, defined as

$$\Lambda = \frac{E}{(1-\nu^2)\sigma_{rep}} \frac{a}{R}, \tag{8}$$

where E and ν are the elastic modulus and Poisson's ratio, respectively. In the initial contact region, Region I, the contact is purely elastic and can be described by Hertz contact theory, which has been covered extensively in the literature [40]. In the fully plastic region, Region III, the contact is solved by a self-similarity solution, and $\overline{H}$ and c^2 takes on constant values, independent of the loading Λ [41–43]. In the region between the purely elastic and the fully plastic contact, Region II, both elastic and plastic effects must be considered to describe the contact behaviour accurately. The relation between the normalised hardness and area parameter to the loading parameter is presented in Fig. 3. No closed-form solution for the normalised hardness or the area parameter has been presented in the literature for Region II. However, Olsson and Larsson [44,45] showed, through extensive finite element analyses of Brinell indentations, that both parameters could be fitted to master curves, dependent on Λ. The normalised hardness could be expressed as a second-degree polynomial of $ln\Lambda$. Combining the solution in all the three contact regions gives the normalised hardness as

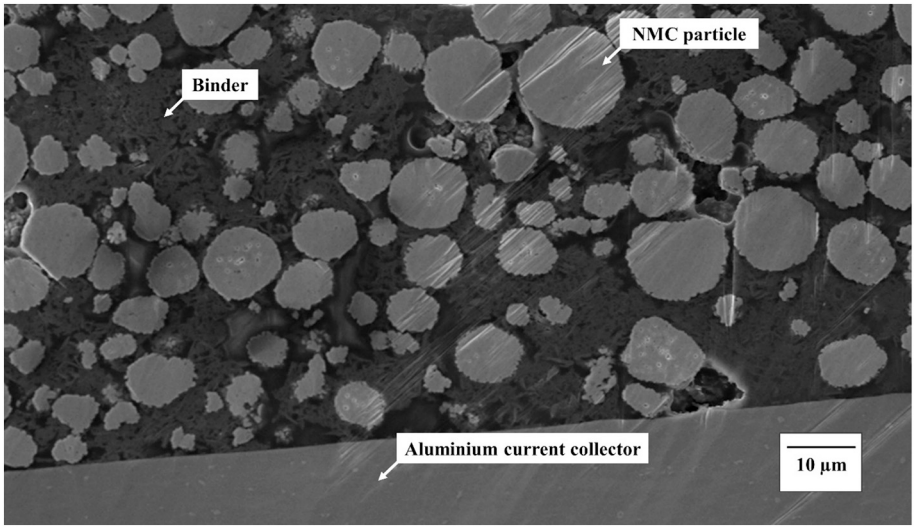


Fig. 2. A SEM image displaying the polished indentation surface of the electrode.

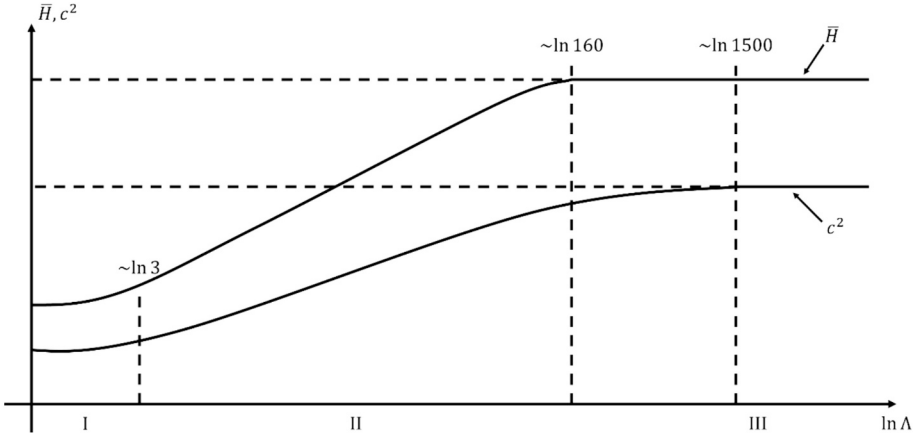


Fig. 3. The normalised hardness and area parameter as a function of the loading parameter Λ in the three loading regions.

$$\overline{H} = \begin{cases} \dfrac{4}{3\pi}\Lambda & \Lambda \leq 3 \\ \overline{H}_{max} - 0.0965(\ln\Lambda - \ln 160)^2 & 3 \leq \Lambda \leq 160 \\ \overline{H}_{max} & \Lambda \geq 160 \end{cases} \tag{9}$$

with $\overline{H}_{max} = 3$. The area parameter could be expressed as a third-degree polynomial of $ln\Lambda$, where the area parameter in all three regions is given by

$$c^2 = \begin{cases} 0.5 & \Lambda < 4 \\ 1.1355x + 0.519x^2 - 0.7245x^3 + 0.5 & 4 \leq \Lambda \leq 1527 \\ 1.43 & \Lambda \geq 1527 \end{cases} \tag{10}$$

where

$$x = \frac{\ln\Lambda - \ln 4}{\ln 1527 - \ln 4}. \tag{11}$$

These relations pertinent to the Brinell indentation can be used to describe contact of spherical particles through the assumption that the contact surface between the spheres is also spherical. The problem can then be divided into two problems of each sphere being indented by a rigid body with a radius of plus/minus the curvature of the contact surface. These two problems can now be equated to a rigid sphere indenting an elastic half-space, giving the same contact force and contact area in the combined solution. The relations can now be solved for a range of contact forces, giving the relation between the contact force/contact area and the indentation depth. Olsson and Larsson [45] could also show that the relation between the contact force/contact area and the displacement normalised with the yield stress and effective radius of the contact pair gave similar results for contacts between spheres of the same size and contacts between spheres of unequal sizes. This allows one master curve of the normalised force-displacement relation to be used in the contact model for all particle contacts. The shape of this master curve was accurately captured by a four-parameter power function on the form

$$\overline{F}\left(\frac{h}{R^*}\right) = \overline{F}_1\left(\frac{h}{R^*}\right)^{\alpha_1} + \overline{F}_2\left(\frac{h}{R^*}\right)^{\alpha_2} \tag{12}$$

with

$$\overline{F}_i = \frac{F_i}{\sigma_Y R^{*2-\alpha_i}} \tag{13}$$

which is easily evaluated in the DEM code using the normalised overlap of the particles in the contact pair. For the complete derivation and motivation of these contact relations, the reader is referred to Olsson and Larsson's work [45]. Unloading is performed in an elastic manner, following Hertz contact theory, as described in our previous study [36].

To investigate the impact of the proposed particle contact model, the same modelling framework as presented in our previous study was used [36]. The code used in the modelling framework is an in-house DEM code with standard DEM formulations. The framework uses an in-plane RVE to represent the active layer of the positive electrode. 5000 discrete elements are used representing the active particles and a rigid surface is placed in the bottom of the RVE representing the current collector. Two contact models are implemented in the framework, representing contact between active particles and particles separated by the CBD.

The simulation takes place in three main steps. Initially, the NMC particles are randomly packed to generate an uncalendered layer. After the random packing, the adhesion of the CBD is enabled to create the bonded layer. The layer is, after that, calendered by compressing the layer to a prescribed height using a rigid surface, which is then removed. Finally, the evaluation of in-plane unloading stiffness or in-plane relaxation is performed. The in-plane unloading stiffness is evaluated by prescribing a strain in one direction of the periodic boundary conditions and recording the stress response over small unloadings. A similar method is used to evaluate the relaxation which is presented further down in this article. The RVE and the main steps of the modelling framework are shown in Fig. 4. A fully detailed description of the modelling framework is given in [36].

A reference simulation case was adapted from the previous study, which would act as a baseline for comparisons with our new model. The reference simulation used the experimentally measured force-overlap relation for the particle contact, described in [36], with the NMC material using a Young's modulus of $E = 140$ GPa and a Poisson's ratio of $\nu = 0.3$. All three compared simulations use the same PSD for the active particles which is provided in Fig. 1. The CBD contact is modelled as a cylinder compressed and sheared between the two particles, where its dimensions (radius and thickness) are dependent on the radius of one of the particles in the contact pair. The relation between the binder thickness b_t and the particle radius R was set to $\frac{b_t}{R} = 0.5$, and the relation between the binder radius b_r and the particle radius was set to $\frac{b_r}{R} = 1.75$. The CBD's material was purely elastic with a Young's modulus of $E = 2$ GPa and a Poisson's ratio of $\nu = 0.3$. This reference case was adapted to our study by changing the contact model between the particles. The reference case was compared to two cases using the proposed elastic-plastic contact model with two sets of material parameters. The two sets of material properties used are from our experimental indentation study and from indentation studies of the same active material, found in the literature. The two sets of material properties can be found in Table 1 as Material 1 and Material 2 respectively. The analysis investigates the impact of the new contact model on the calendering process as well as the measurement of in-plane unloading stiffness in compression and

tension. In order to account for stochastic variations, four simulations have been performed for each case.

Applying the new particle contact model results in an increased calendering pressure for both sets of material properties, as compared to the reference simulation, which can be seen in Fig. 5 (a). Comparting the two materials in the new contact model, it is apparent in Fig. 5 (a) that Material 2, with a higher modulus and yield strength, also results in an increased calendering pressure. The new contact model also captures the pressure sensitivity of the layers in-plane stiffness, with an increasing stiffness at increasing compression levels. The increase in stiffness at increased compression levels is however not as prevalent as for the reference simulation, which can be observed in Fig. 5 (b).

By plotting the number of particle contacts during the measurement of in-plane stiffness, shown in Fig. 6, it is evident that slope of stiffness increase, at increasing compression levels, is proportional to the increase in particle contacts. It is also evident that the initial number of particle contacts (at zero strain), after calendering, is higher for the new particle contact model. This increase in number of particle contacts follows an increased elastic unloading region in the new particle contact model with a more realistic unloading stiffness.

3.2. Viscoelasticity in the binder domain

The mechanical properties of the active layer show time-dependent behaviour, as shown in several experimental studies [21,26,29,30]. The time dependency of the electrode layer stems from the viscoelastic constitutive behaviour of the CBD. One method of measuring the time-dependent behaviour is through relaxation tests, as seen in [29,30]. The time-dependent behaviour was incorporated in our simulation framework by including viscoelasticity, and disregarding plasticity, in the binder domain. Apart from the new constitutive behaviour, the binder domain was modelled in the same manner as in our previous work [36], i.e. as a cylinder which is compressed and sheared between the two particles. Through the viscoelastic correspondence principle, the elastic force-overlap expression of the binder domain can be rewritten in time-dependent form by replacing the Young's modulus with its time-dependent counterpart $E(t)$, providing the assumption that the Poisson's ratio ν is time-independent. The time-dependent force-overlap expression in the normal direction is given by

$$F_b(h,t) = \frac{(1-\nu)A}{(1+\nu)(1-2\nu)} \int_0^t E(t-\tau) \frac{d}{d\tau} \frac{h(\tau)+b_t}{b_t} d\tau, \tag{14}$$

where A is the cross-sectional area of the binder following the binder radius b_r, b_t is the binder thickness and $h(t)$ is the time-dependent overlap. The radius and thickness of the binder cylinder is set as relations to the radius of one of the particles in the contact pair, as mentioned previously. The time-dependent Young's modulus is assumed to be well described by a generalised Maxwell model, expressed by a Prony series through

$$E(t) = E_0 \left[1 - \sum_{i=1}^{N} \alpha_i \left(1 - exp\left(-\frac{t}{\tau_i} \right) \right) \right], \tag{15}$$

where E_0 is the instantaneous modulus, and α_i and τ_i are the parameters in the Maxwell elements, where α_i is the stiffness decrease ratio related to the relaxation time τ_i. The number of maxwell elements, N, must be adapted to the experimental relaxation data to accurately describe the relaxation behaviour. Differentiating the expression in Eqs. (14) and (15) gives the force increment ΔF dependent on the overlap increment Δh and the time increment Δt. The complete derivation of the incremental time-dependent force-overlap expression is presented by Olsson and Jelagin [47], where it is applied on viscoelastic spherical particles. The tangential force-displacement relation is derived similarly as for the normal direction, resulting in the relation

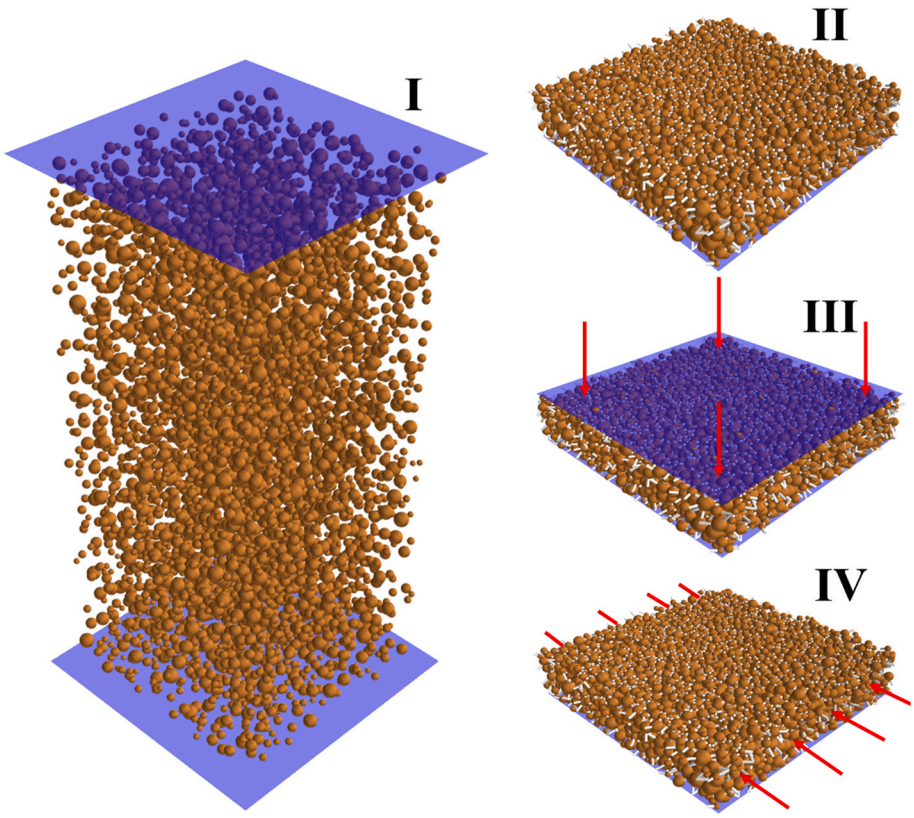


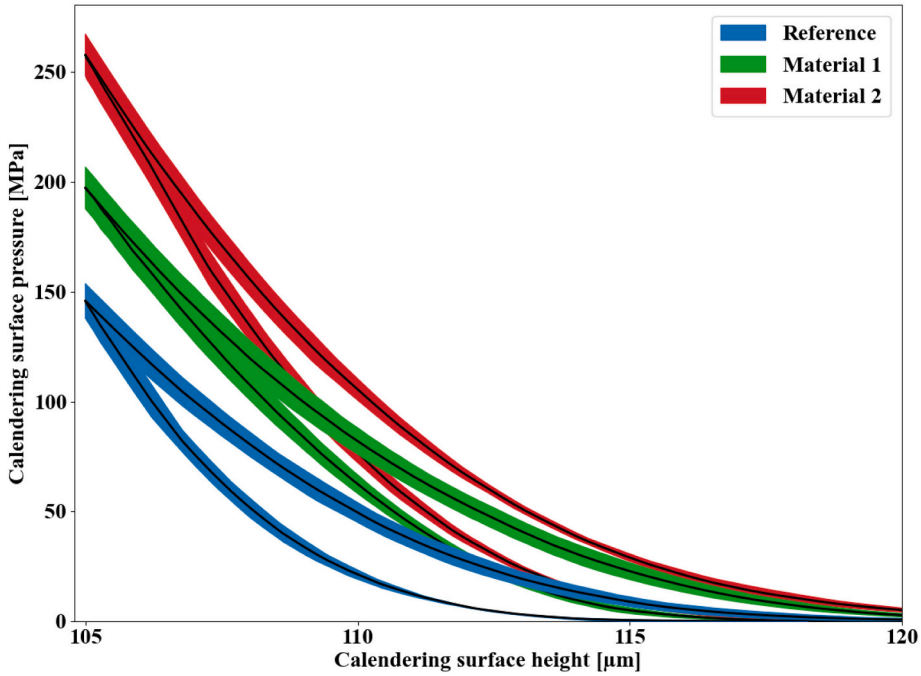
Fig. 4. The RVE of the positive electrode for the different steps in the simulation process: (I) random packing, (II) uncalendered electrode layer, (III) calendering process, (IV) in-plane mechanical loading and relaxation. Figure adapted from [36].

Table 1
Material properties for the active material.

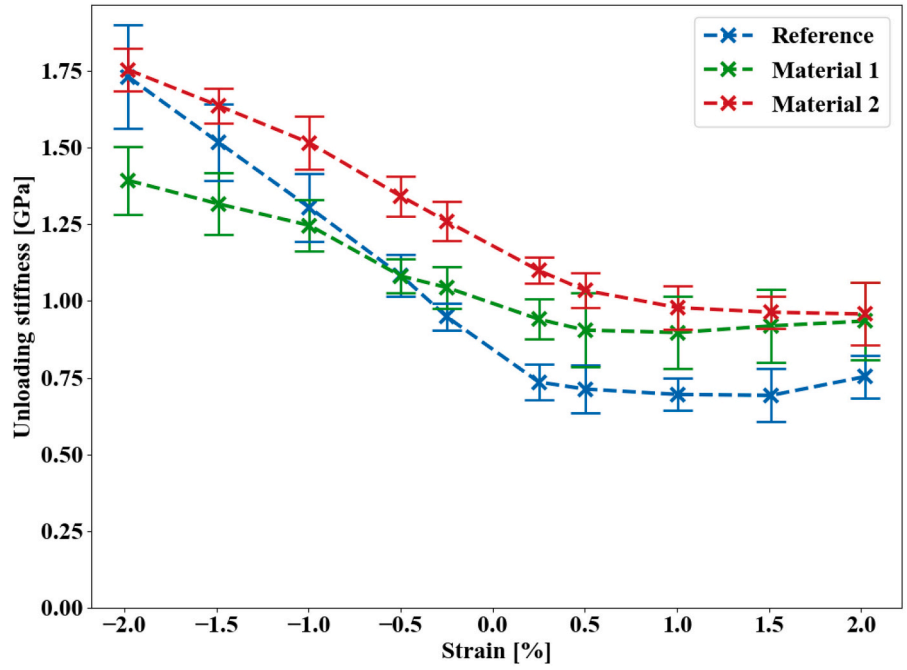
Parameter	Material 1	Material 2 [46]
Young's modulus [GPa]	50	140
Poisson's ratio [−]	0.3	0.3
Yield strength [GPa]	2.4	3.3

$$F_t(u,t) = \frac{A}{2(1+\nu)} \int_0^t E(t-\tau) \frac{d}{d\tau} \frac{u(\tau)}{b_t} d\tau, \tag{16}$$

where $u(t)$ is the time-dependent tangential displacement. A dampening in the binder domain contact model, which was referred to in the previous study [36], was implemented in the manner described above with the Prony series parameters $\alpha_{Damper} = 0.25$, $\tau_{Damper} = 0.001$ s. When the Prony series parameters now are expanded to describe the viscoelasticity of the CBD, the damper must be accounted for to keep the relation



(a)



(b)

Fig. 5. (a) Calendering pressure to calendering surface height and, (b) in-plane unloading stiffness at various strain levels for the three materials. Results show mean and standard deviation with a comparison to a reference simulation, taken from [36].

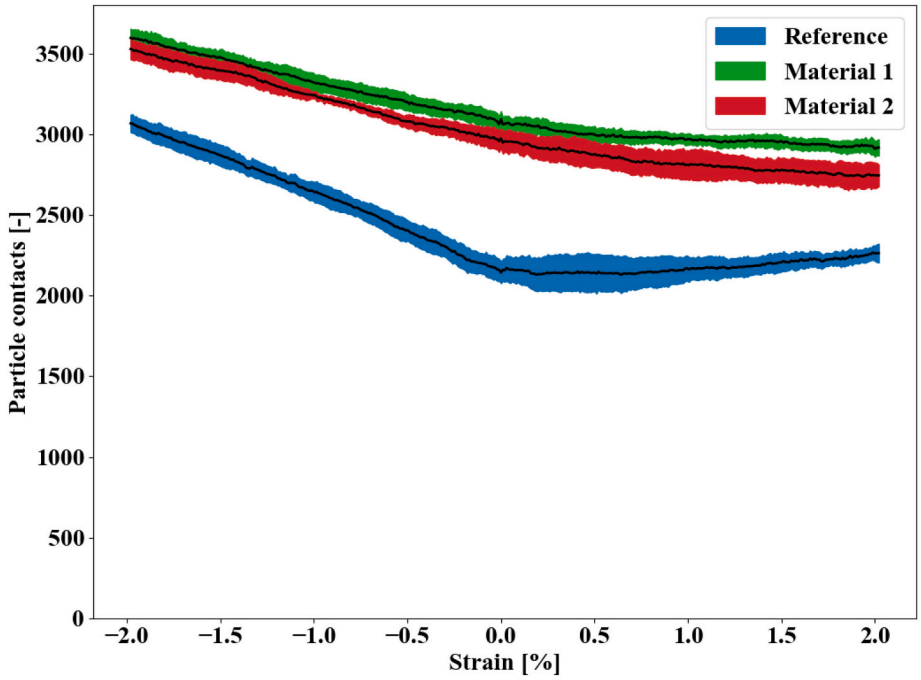


Fig. 6. Number of particle contacts at strain levels during mechanical loading. Results show mean and standard deviation with a comparison to a reference simulation, taken from [36].

between the instantaneous stiffness and the relaxed stiffness. This is done by decreasing the viscoelastic Prony series parameters with the same factor as the damper, in this case 25%. Therefore, the applied stiffness ratios α_i are scaled by a factor of 0.75. N.B. the stiffness ratios presented below are without scaling. The relaxation time, related to the stiffness ratios, must also be magnitudes larger than the relaxation time of the damper to not be influenced.

Data for the viscoelastic properties of the CBD are sparse in the literature. Initially, the relaxation experiments performed by Santimetaneedol et al. [21] on PVDF films have been fitted to the generalised Maxwell model with two Maxwell elements. The fitting of the experimental results gave the parameters $E_0 = 2$ GPa, $\alpha_1 = 0.052$, $\tau_1 = 1700$ s, $\alpha_2 = 0.11$, $\tau_2 = 38000$ s, and will be referenced to as Prony series 1. It should be noted that their experiments were performed on the pure PVDF, not the PVDF, CB mixture found in the CBD. The presence of CB in the CBD indeed influences its mechanical properties, as shown in experiments [23,26,48]. This is also likely to be the case for the viscoelastic behaviour. The new particle contact model, presented above, was used with the material properties of Material 1 in Table 1.

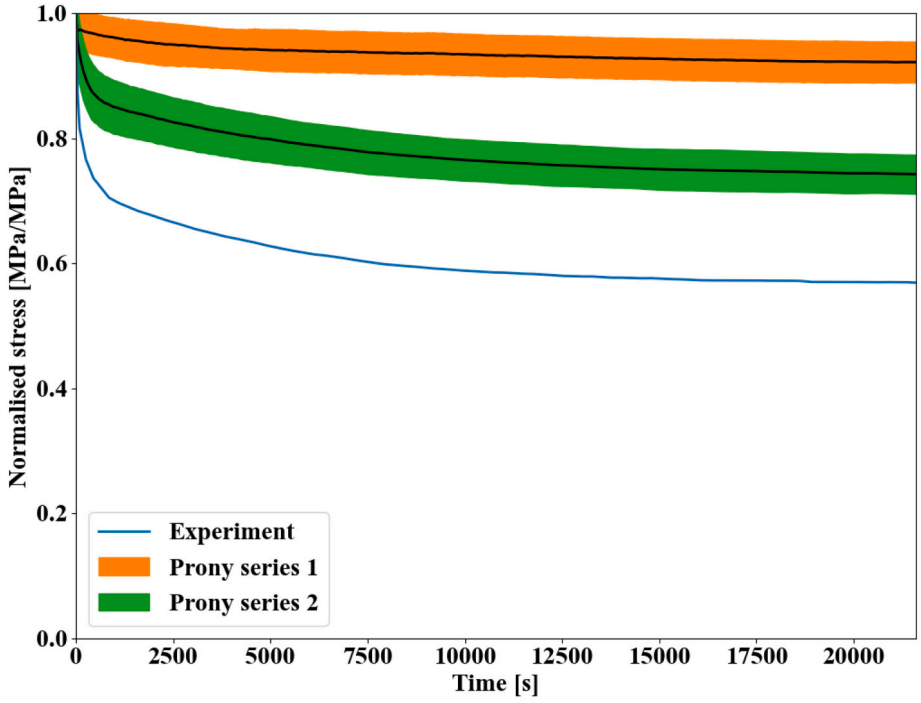
The relaxation simulations are performed by uniaxially loading the layer, either in compression or tension, to a prescribed strain, which is then held for a specified time while the stress in the loading direction is recorded. The stress is normalised against the difference in stress increase during loading. Precursing the relaxation process, the layer is packed and calendered, as described in the framework methodology. To avoid residual viscoelastic stresses from the calendering process, the layer is allowed to relax for $2{\cdot}10^5$ s, which is more than five times the largest relaxation time in the Maxwell elements. To validate the results, the simulations were compared to the relaxation experiment of the full cathode active layer performed by Gupta et al. [29]. In the experiment, the in-plane strain, in tension and compression, was 1.65% and was held for six hours. The strain load was applied instantaneously, relative to the lowest relaxation time.

To perform the simulations with reasonable computational resources, the time constants of the Prony series, strain rate and the hold time in the relaxation were scaled down with a factor of 10^{-2}. This scaling accounted for the magnitude of the relaxation time in the damper element, ensuring that the damper did not influence the viscoelastic behaviour. As the viscoelastic relaxation is the only time-dependent process, re-scaling these time constants will not affect any other system properties, thus providing accurate viscoelastic results. Mass scaling of the particles was also applied to increase the critical timestep. As the relaxation is a quasistatic process, mass scaling will enable increased timesteps without affecting the system's behaviour.

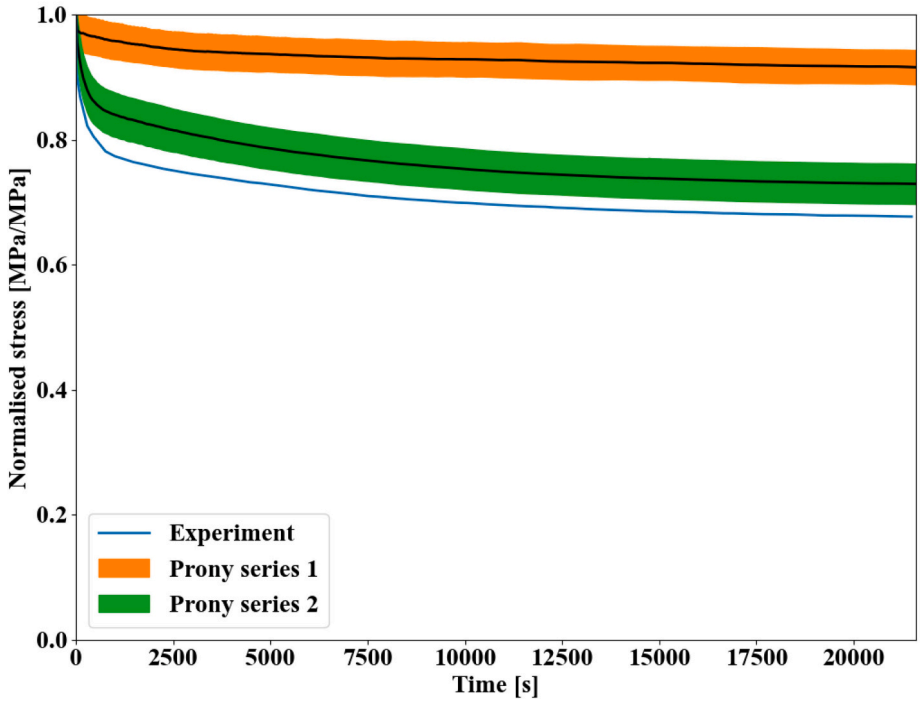
The normalised relaxation stress over time of both the experimental results and the simulations can be seen in Fig. 7, where the experimental results show a relaxation of 41% and 33% in tension and compression, respectively. The degree of relaxation in the simulations was lower, with a 7.8% and 8.4% relaxation in tension and compression, respectively. This discrepancy is believed to stem from the viscoelastic properties of the CBD. These results show that neither the magnitude of relaxation nor the more prominent relaxation in tension than in compression is captured.

In order to evaluate if our model could capture the relaxations levels observed in the experiments more accurately, the properties of the Maxwell elements were adapted to have the same magnitude in both relaxation degree and relaxation time as the relaxation modulus from the experiments. The values adapted in the Prony series were the average values in the fitting relaxation modulus function in compression and tension from the experiments [29]. The determined values for the adapted Prony series were $\alpha_1 = 0.2, \tau_1 = 200$ s, $\alpha_2 = 0.2, \tau_2 = 6000$ s and will be referenced as Prony series 2. The relaxation simulation was again carried out in the same manner.

The relaxation behaviour with the adapted Prony series, seen in Fig. 7, gives a more accurate representation of the relaxation behaviour observed in the experiments. The simulated relaxation was 26% and 27% in tension and compression respectively. The notable difference in relaxation between tension and compression seen in the experiments was, however, still not captured. In reference to these results, it should, indeed, be noted that the relaxation properties used for the CBD stem from measurements of the full cathode layer in both compression and tension, and not only the CBD. A more accurate input of the CBDs time dependent properties might be to only use the experimental results in tension, as the behaviour of the CBD is the main influences of the



(a)



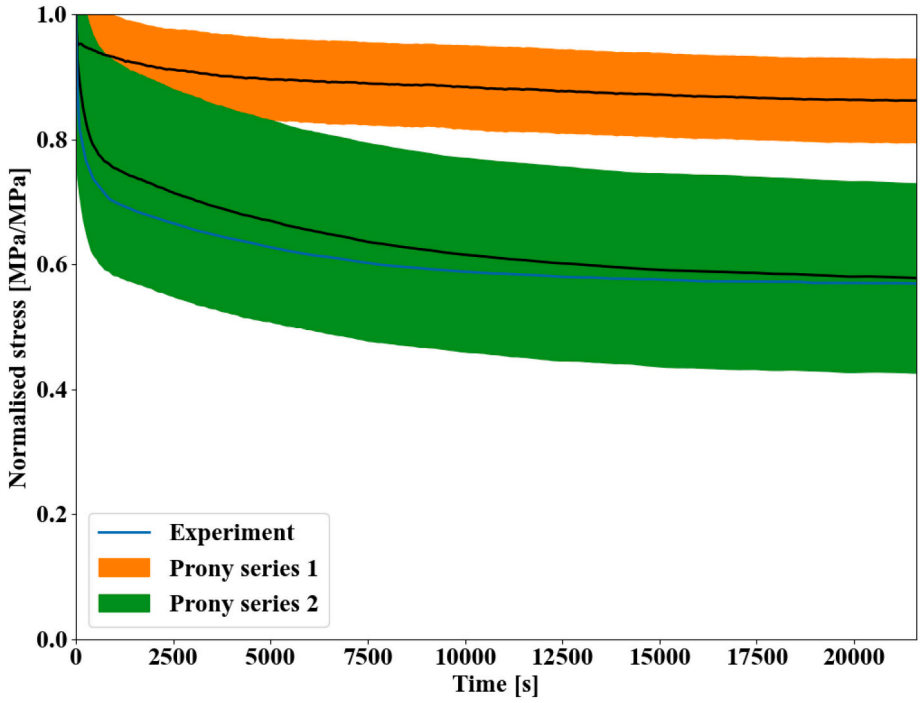
(b)

Fig. 7. Relaxation behaviour of the layer in (a) tension and (b) compression for both sets of Prony series. Results show mean and standard deviation.

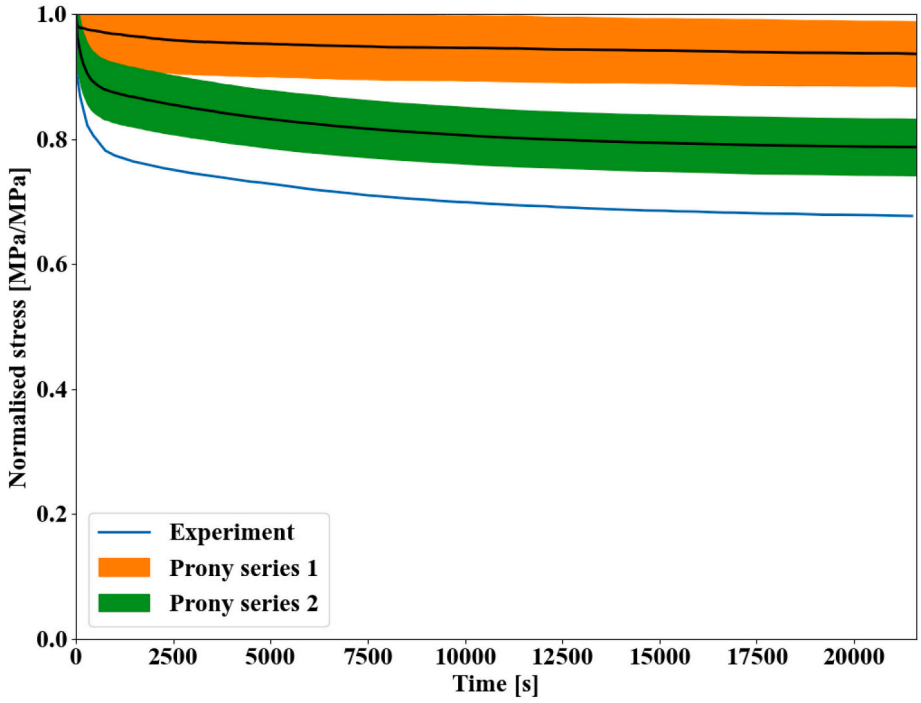
behaviour in tension. The contact model for the binder also only obtains linear viscoelastic properties, something which perhaps will not capture the true behaviour of the porous CBD, which itself might be pressure sensitive. To gain more accurate model inputs, the viscoelastic properties of the CBD must be measured experimentally, something which has not been performed in the literature. The outcome of the relaxation degree is also a product of the normalisation procedure. After the calendering and resting stage of the simulation, the layer possesses residual compressive stresses in the in-plane directions. When normalising with the change in stresses, and thus accounting for the initial compressive stress, the relaxation in compression is increased and the relaxation in tension is decreased. If, instead, the results were normalised with the stress value after loading and disregarding the initial stress state, the relaxation in tension would be more pronounced compared to

the relaxation in compression, as can be seen in Fig. 8. This normalisation method will, however, also increase the spread of results for the simulation in tension.

The impact of strain load on the degree of relaxation was also investigated. This by performing the simulation, described above, but with relaxation at strain levels of 1% and 2% in tension and compression. The impact of strain levels on the relaxation is miniscule both in tension and compression, which can be seen in Fig. 9. The only trend seen was a slight reduction of relaxation in compression at increased strain levels. This is caused by the increased number of particle contacts, which do not have a time-dependent contact behaviour.

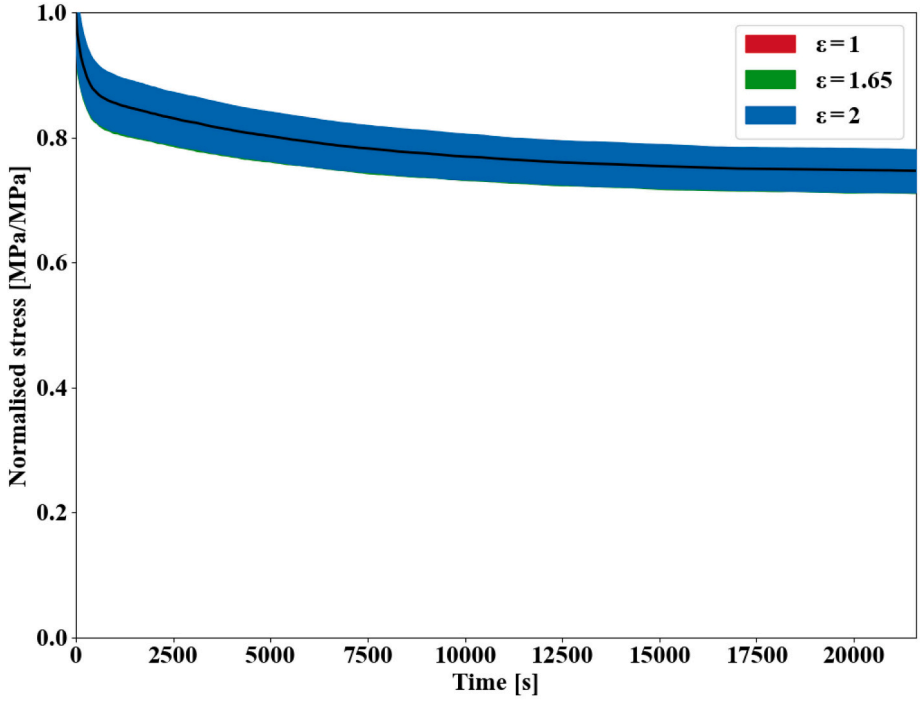


(a)

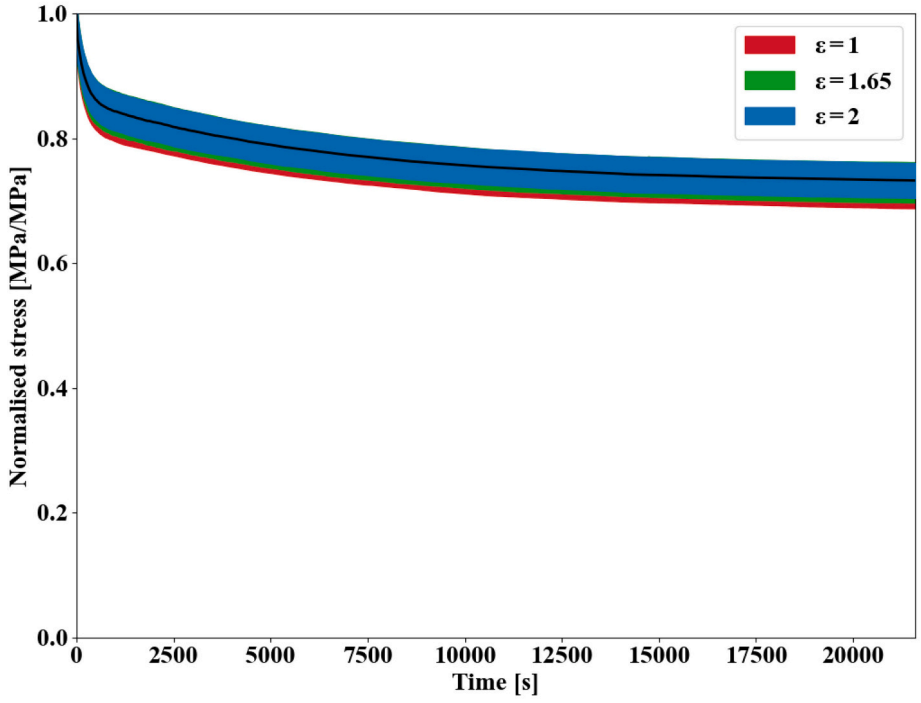


(b)

Fig. 8. Relaxation behaviour of the layer in (a) tension and (b) compression for both sets of Prony series with stress normalisation disregarding the initial stress state. Results show mean and standard deviation.



(a)



(b)

Fig. 9. Relaxation of layer at various strain levels in (a) tension and (b) compression. Results show mean and standard deviation.

4. Conclusions

This study expanded a DEM modelling framework investigating the mechanical properties of a LIB cathode active layer from a previous study. A new contact model for the active material and viscoelasticity in the CBD was implemented into the modelling framework to fill a gap in the literature. The main conclusions of the study were:

- A more theoretically motivated contact model for the active material provided similar properties to the entire active layer, apart from a less pronounced increase of in-plane stiffness at increased compression levels.
- The model can qualitatively capture the relaxation behaviours of the active layer in both tension and compression.

CRediT authorship contribution statement

Axel Lundkvist: Conceptualization, Methodology, Software, Formal analysis, Writing – original draft, Writing – review & editing, Visualization. **Per-Lennart Larsson:** Conceptualization, Writing – original draft, Writing – review & editing, Supervision. **Anand H.S. Iyer:** Investigation, Writing – review & editing. **Erik Olsson:** Conceptualization, Software, Writing – original draft, Writing – review & editing, Supervision, Funding acquisition.

Declaration of competing interest

The authors declare that they have no known competing financial interests or personal relationships that could have appeared to influence the work reported in this paper.

Data availability

The code is shared on GitHub: https://github.com/axlun/DEMsim.

Acknowledgements

The authors would like to acknowledge Assoc. Prof. Christopher Hulme for aiding the measurement of particle size distribution, Prof. Peter Gudmundson and Prof. Artem Kulachenko for helpful discussions, and Energimyndigheten (the Swedish Energy Agency) for financing the project through the grant 46558-1.

References

[1] M. Li, J. Lu, Z. Chen, K. Amine, 30 years of Lithium-ion batteries, Adv. Mater. 30 (33) (Aug. 2018) 1800561, https://doi.org/10.1002/adma.201800561.
[2] J.C. Stallard, et al., Mechanical properties of cathode materials for lithium-ion batteries, Joule 6 (5) (2022) 984–1007, https://doi.org/10.1016/j.joule.2022.04.001.
[3] A. Mukhopadhyay, B.W. Sheldon, Deformation and stress in electrode materials for Li-ion batteries, Prog. Mater. Sci. 63 (January) (2014) 58–116, https://doi.org/10.1016/j.pmatsci.2014.02.001.
[4] J.S. Edge, et al., Lithium ion battery degradation: what you need to know, Phys. Chem. Chem. Phys. 23 (14) (2021) 8200–8221, https://doi.org/10.1039/d1cp00359c.
[5] D. Schreiner, A. Klinger, G. Reinhart, Modeling of the calendering process for lithium-ion batteries with DEM simulation, Procedia CIRP 93 (2020) 149–155, https://doi.org/10.1016/j.procir.2020.05.158.
[6] D. Schreiner, J. Lindenblatt, F.J. Günter, G. Reinhart, DEM simulations of the Calendering process: parameterization of the electrode material of Lithium-ion batteries, Procedia CIRP 104 (2021) 91–97, https://doi.org/10.1016/j.procir.2021.11.016.
[7] D. Schreiner, J. Lindenblatt, R. Daub, G. Reinhart, Simulation of the Calendering process of NMC-622 cathodes for Lithium-ion batteries, Energ. Technol. (2022), https://doi.org/10.1002/ente.202200442.
[8] C. Sangrós Giménez, B. Finke, C. Schilde, L. Froböse, A. Kwade, Numerical simulation of the behavior of lithium-ion battery electrodes during the calendaring process via the discrete element method, Powder Technol. 349 (2019) 1–11, https://doi.org/10.1016/j.powtec.2019.03.020.
[9] M. Lippke, J. Meister, C. Schilde, A. Kwade, Preheating of Lithium-ion battery electrodes as basis for heated Calendering—a numerical approach, Processes 10 (8) (2022), https://doi.org/10.3390/pr10081667.
[10] A.C. Ngandjong, et al., Investigating electrode calendering and its impact on electrochemical performance by means of a new discrete element method model: towards a digital twin of Li-ion battery manufacturing, J. Power Sources 485 (2021) 229320, https://doi.org/10.1016/j.jpowsour.2020.229320.
[11] J. Xu, et al., Lithium ion battery electrode manufacturing model accounting for 3D realistic shapes of active material particles, J. Power Sources 554 (October) (2022) 2023, https://doi.org/10.1016/j.jpowsour.2022.232294.
[12] J. Xu, et al., Computational model for predicting particle fracture during electrode calendering, Batter. Supercaps (2023), https://doi.org/10.1002/batt.202300371.
[13] J. Zhang, J. Sun, H. Huang, Z. Yuan, Influence of calendering process on the structural mechanics and heat transfer characteristics of lithium-ion battery electrodes via DEM simulations, Particuology 85 (Feb. 2024) 252–267, https://doi.org/10.1016/j.partic.2023.06.015.
[14] J. Zhang, H. Huang, J. Sun, Investigation on mechanical and microstructural evolution of lithium-ion battery electrode during the calendering process, Powder Technol. 409 (May) (2022) 117828, https://doi.org/10.1016/j.powtec.2022.117828.
[15] C. Sangrós Giménez, B. Finke, C. Nowak, C. Schilde, A. Kwade, Structural and mechanical characterization of lithium-ion battery electrodes via DEM simulations, Adv. Powder Technol. 29 (10) (2018) 2312–2321, https://doi.org/10.1016/j.apt.2018.05.014.
[16] C. Sangrós Giménez, C. Schilde, L. Froböse, S. Ivanov, A. Kwade, Mechanical, electrical, and ionic behavior of Lithium-ion battery electrodes via discrete element method simulations, Energ. Technol. 8 (2) (2020) 1–10, https://doi.org/10.1002/ente.201900180.
[17] C. Sangrós Giménez, L. Helmers, C. Schilde, A. Diener, A. Kwade, Modeling the electrical conductive paths within all-solid-state battery electrodes, Chem. Eng. Technol. 43 (5) (2020) 819–829, https://doi.org/10.1002/ceat.201900501.
[18] M. Lippke, et al., Simulation of structure formation during drying of Lithium-ion battery electrodes using discrete element method, Energ. Technol. 2200724 (2022), https://doi.org/10.1002/ente.202200724.
[19] C. Lischka, H. Nirschl, Calibration of Li-ion cathode materials for discrete element method simulations, Energ. Technol. 2200849 (2022) 2200849, https://doi.org/10.1002/ente.202200849.
[20] M. Kespe, H. Nirschl, Numerical simulation of lithium-ion battery performance considering electrode microstructure, Int. J. Energy Res. 39 (15) (2015) 2062–2074, https://doi.org/10.1002/er.3459.
[21] A. Santimetaneedol, R. Tripuraneni, S.A. Chester, S.P.V. Nadimpalli, Time-dependent deformation behavior of polyvinylidene fluoride binder: implications on the mechanics of composite electrodes, J. Power Sources 332 (2016) 118–128, https://doi.org/10.1016/j.jpowsour.2016.09.102.
[22] S. Ono, K. Shiraishi, Y. Kishimoto, Y. Kobayashi, H. Yamazaki, T. Nomoto, Simple estimation of creep properties of negative electrode for Lithium-ion battery, Zair. Soc. Mater. Sci. Japan 71 (12) (2022) 989–996, https://doi.org/10.2472/JSMS.71.989.
[23] Z. Chen, L. Christensen, J.R. Dahn, A study of the mechanical and electrical properties of a polymer/carbon black binder system used in battery electrodes, J. Appl. Polym. Sci. 90 (7) (2003) 1891–1899, https://doi.org/10.1002/app.12863.
[24] Z. Chen, L. Christensen, J.R. Dahn, Comparison of PVDF and PVDF-TFE-P as binders for electrode materials showing large volume changes in Lithium-ion batteries, J. Electrochem. Soc. 150 (8) (2003) A1073, https://doi.org/10.1149/1.1586922.
[25] Z. Chen, L. Christensen, J.R. Dahn, Study of the mechanical and electrical properties of carbon/poly(vinylidene fluoride-tetrafluoroethylene-propylene) films crosslinked with triethylenetetramine: possible application as binder for lithium-ion battery electrodes, J. Appl. Polym. Sci. 91 (5) (2004) 2949–2957, https://doi.org/10.1002/app.13504.
[26] H. Hu, B. Tao, Y. He, S. Zhou, Effect of conductive carbon black on mechanical properties of aqueous polymer binders for secondary battery electrode, Polymers (Basel). 11 (9) (2019), https://doi.org/10.3390/polym11091500.
[27] A.H.S. Iyer, P. Gupta, P. Gudmundson, A. Kulachenko, Measuring microscale mechanical properties of PVdF binder phase and the binder-particle interface using micromechanical testing, Mater. Sci. Eng. A 881 (May) (2023) 145352, https://doi.org/10.1016/j.msea.2023.145352.
[28] L.S. de Vasconcelos, R. Xu, J. Li, K. Zhao, Grid indentation analysis of mechanical properties of composite electrodes in Li-ion batteries, Extrem. Mech. Lett. 9 (2016) 495–502, https://doi.org/10.1016/j.eml.2016.03.002.
[29] P. Gupta, I.B. Üçel, P. Gudmundson, E. Olsson, Characterization of the constitutive behavior of a cathode active layer in Lithium-ion batteries using a bending test method, Exp. Mech. 60 (6) (2020) 847–860, https://doi.org/10.1007/s11340-020-00613-5.
[30] B. Üçel, P. Gupta, P. Gudmundson, Experimental determination of the constitutive properties of a graphite anode layer in lithium-ion batteries using a bending test method, J. Energy Storage 46 (February 2021) (2022) 103845, https://doi.org/10.1016/j.est.2021.103845.
[31] C. Zhang, J. Xu, L. Cao, Z. Wu, S. Santhanagopalan, Constitutive behavior and progressive mechanical failure of electrodes in lithium-ion batteries, J. Power Sources 357 (2017) 126–137, https://doi.org/10.1016/j.jpowsour.2017.04.103.
[32] M. Ebner, F. Geldmacher, F. Marone, M. Stampanoni, V. Wood, X-ray tomography of porous, transition metal oxide based Lithium ion battery electrodes, Adv. Energy Mater. 3 (7) (2013) 845–850, https://doi.org/10.1002/aenm.201200932.
[33] T. Bond, R. Gauthier, S. Gasilov, J.R. Dahn, In-situ computed tomography of particle microcracking and electrode damage in cycled NMC622/graphite pouch cell batteries, J. Electrochem. Soc. 169 (8) (2022) 080531, https://doi.org/10.1149/1945-7111/ac8a22.
[34] T. Bond, R. Gauthier, A. Eldesoky, J. Harlow, J.R. Dahn, In situ imaging of electrode thickness growth and electrolyte depletion in single-crystal vs polycrystalline LiNixMnyCozO 2 /graphite pouch cells using multi-scale computed tomography, J. Electrochem. Soc. 169 (2) (2022) 020501, https://doi.org/10.1149/1945-7111/ac4b83.
[35] V. Nagda, A. Kulachenko, S.B. Lindström, Image-based 3D characterization and reconstruction of heterogeneous battery electrode microstructure, Comput. Mater. Sci. 223 (March) (2023), https://doi.org/10.1016/j.commatsci.2023.112139.
[36] A. Lundkvist, P.L. Larsson, E. Olsson, A discrete element analysis of the mechanical behaviour of a lithium-ion battery electrode active layer, Powder Technol. 425 (March) (2023) 118574, https://doi.org/10.1016/j.powtec.2023.118574.
[37] W.C. Oliver, G.M. Pharr, An improved technique for determining hardness and elastic modulus using load and displacement sensing indentation experiments, J. Mater. Res. 7 (6) (1992) 1564–1583, https://doi.org/10.1557/jmr.1992.1564.
[38] D. Tabor, The Hardness of Metals, Clarendon, Oxford, 1951.
[39] K.L. Johnson, The correlation of indentation experiments, J. Mech. Phys. Solids 18 (2) (1970) 115–126, https://doi.org/10.1016/0022-5096(70)90029-3.

[40] H. Hertz, Ueber die Berührung fester elastischer Körper, J. Fur Die Reine und Angew. Math. 1882 (92) (1882) 156–171, https://doi.org/10.1515/crll.1882.92.156.
[41] S. Biwa, B. Storåkers, An analysis of fully plastic Brinell indentation, J. Mech. Phys. Solids 43 (8) (1995) 1303–1333, https://doi.org/10.1016/0022-5096(95)00031-D.
[42] B. Storåkers, S. Biwa, P.L. Larsson, Similarity analysis of inelastic contact, Int. J. Solids Struct. 34 (24) (1997) 3061–3083, https://doi.org/10.1016/S0020-7683(96)00176-X.
[43] B. Storåkers, Local contact behaviour of Viscoplastic particles, in: IUTAM Symposium on Mechanics of Granular and Porous Materials 1996, 1997, pp. 173–184, https://doi.org/10.1007/978-94-011-5520-5_16.
[44] E. Olsson, P.L. Larsson, On the appropriate use of representative stress quantities at correlation of spherical contact problems, Tribol. Lett. 50 (2) (2013) 221–232, https://doi.org/10.1007/s11249-013-0114-1.
[45] E. Olsson, P.L. Larsson, A unified model for the contact behaviour between equal and dissimilar elastic-plastic spherical bodies, Int. J. Solids Struct. 81 (2016) 23–32, https://doi.org/10.1016/j.ijsolstr.2015.10.004.
[46] N. Sharma, D. Meng, X. Wu, L.S. de Vasconcelos, L. Li, K. Zhao, Nanoindentation measurements of anisotropic mechanical properties of single crystalline NMC cathodes for Li-ion batteries, Extrem. Mech. Lett. 58 (2022) 101920, https://doi.org/10.1016/j.eml.2022.101920.
[47] E. Olsson, D. Jelagin, A contact model for the normal force between viscoelastic particles in discrete element simulations, Powder Technol. 342 (2019) 985–991, https://doi.org/10.1016/j.powtec.2018.10.022.
[48] F. Kong, M. Chang, Z. Wang, Comprehensive analysis of mechanical properties of CB/SiO2/PVDF composites, Polymers (Basel). 12 (1) (2020) 1–13, https://doi.org/10.3390/polym12010146.